

# Quantitative Regional and Ultrastructural Localization of the Ca<sub>v</sub>2.3 Subunit of R-type Calcium Channel in Mouse Brain

Laxmi Kumar Parajuli,<sup>1,2</sup> Chikako Nakajima,<sup>3,4</sup> Akos Kulik,<sup>5,6</sup> Ko Matsui,<sup>1,2,7</sup> Toni Schneider,<sup>8</sup> Ryuichi Shigemoto,<sup>1,2,9</sup> and Yugo Fukazawa<sup>1,2,10</sup>

<sup>1</sup>Division of Cerebral Structure, National Institute for Physiological Sciences, Okazaki 444-8787, Japan, <sup>2</sup>Department of Physiological Sciences, The Graduate University for Advanced Studies (SOKENDAI), Okazaki 444-8787, Japan, <sup>3</sup>Faculty of Biology, University of Freiburg, D-79104 Freiburg, Germany, <sup>4</sup>Center for Neuroscience, University of Freiburg, D-79104 Freiburg, Germany, <sup>5</sup>BIOSS Centre for Biological Signalling Studies, University of Freiburg, D-79104 Freiburg, Germany, <sup>6</sup>Department of Physiology II, University of Freiburg, D-79104 Freiburg, Germany, <sup>7</sup>Precursory Research for Embryonic Science and Technology (PRESTO), Japan Science and Technology Agency, Kawaguchi 333-0012, Japan, <sup>8</sup>Institute of Neurophysiology, University of Cologne, D-50931 Cologne, Germany, <sup>9</sup>Solutions Oriented Research for Science and Technology (SORST), Japan Science and Technology Agency, Kawaguchi 333-0012, Japan, and <sup>10</sup>Core Research for Evolutional Science and Technology (CREST), Japan Science and Technology Agency, Chiyoda-ku, Tokyo 102-0075, Japan

R-type calcium channels (RTCCs) are well known for their role in synaptic plasticity, but little is known about their subcellular distribution across various neuronal compartments. Using subtype-specific antibodies, we characterized the regional and subcellular localization of Ca<sub>v</sub>2.3 in mice and rats at both light and electron microscopic levels. Ca<sub>v</sub>2.3 immunogold particles were found to be predominantly presynaptic in the interpeduncular nucleus, but postsynaptic in other brain regions. Serial section analysis of electron microscopic images from the hippocampal CA1 revealed a higher density of immunogold particles in the dendritic shaft plasma membrane compared with the pyramidal cell somata. However, the labeling densities were not significantly different among the apical, oblique, or basal dendrites. Immunogold particles were also observed over the plasma membrane of dendritic spines, including both synaptic and extrasynaptic sites. Individual spine heads contained <20 immunogold particles, with an average density of ~260 immunoparticles per  $\mu\text{m}^3$  spine head volume, in accordance with the density of RTCCs estimated using calcium imaging (Sabatini and Svoboda, 2000). The Ca<sub>v</sub>2.3 density was variable among similar-sized spine heads and did not correlate with the density in the parent dendrite, implying that spines are individual calcium compartments operating autonomously from their parent dendrites.

## Introduction

The R-type calcium channel (RTCC) is a unique member of voltage-gated calcium channel (VGCC) subtypes, as its biophysical properties, such as the membrane voltage and the kinetics for channel activation and inactivation, are distinct from those of typical high-voltage-activated (P/Q-type, N-type, and L-type) or

low-voltage-activated (T-type) (Soong et al., 1993; Williams et al., 1994) classes of VGCCs. Although in some brain regions the molecular identity of RTCC remains somewhat controversial (Tottene et al., 2000; Wilson et al., 2000), the Ca<sub>v</sub>2.3 subunit has been shown to mediate the RTCC current in the hippocampus (Sochivko et al., 2002; Giessel and Sabatini, 2011). Among the 10 VGCC subtypes, the RTCC has attracted special interest in recent years because of its role in neurotransmitter release (Wu et al., 1999; Gasparini et al., 2001), hippocampal synaptic plasticity (Yasuda et al., 2003; Takahashi and Magee, 2009), and functional specificity over other VGCC subunits to dampen synaptic potentials by activating small-conductance calcium-activated potassium (SK) channels (Bloodgood and Sabatini, 2007). However, the subcellular locus of Ca<sub>v</sub>2.3-mediated calcium signaling has not yet been identified.

*In situ* hybridization studies show a robust expression of Ca<sub>v</sub>2.3 messenger RNA in the hippocampus (Soong et al., 1993; Williams et al., 1994), but the protein localization cannot be fully characterized by this technique. Similarly, the subcellular localization of the Ca<sub>v</sub>2.3 protein in hippocampal neurons remains inconsistent with reports of prominent somatic expression (Yokoyama et al., 1995), dendritic localization (Day et al., 1996), and even selective localization to dendritic spines of CA1 pyramidal cells (Bloodgood and Sabatini, 2007). To resolve inconsis-

Received March 8, 2012; revised July 2, 2012; accepted July 30, 2012.

Author contributions: L.K.P. and Y.F. designed research; L.K.P., C.N., and A.K. performed research; T.S. contributed unpublished reagents/analytic tools; L.K.P., C.N., K.M., and Y.F. analyzed data; L.K.P., A.K., R.S., and Y.F. wrote the paper.

This work was supported by funding from Solutions Oriented Research for Science and Technology (SORST), Japan Science and Technology Agency (JST) (to R.S.); Core Research for Evolutional Science and Technology (CREST), JST (to Y.F.); Grant-in-Aid for Scientific Research on Priority Areas—Molecular Brain Sciences (No. 20019031 to R.S. and No. 18022043 to Y.F.); Scientific Research on Priority Areas—Elucidation of Neural Network Function in the Brain (No. 23115520 to Y.F.) from the Ministry of Education, Culture, Sports, Science and Technology of Japan (MEXT); and the Deutsche Forschungsgemeinschaft (SFB 780 A2 to A.K.). We thank Dr. Tsutomu Tanabe and the RIKEN BioResource Center (the National Bio-Resource Project of the MEXT, Japan) for providing us Ca<sub>v</sub>2.3 KO mice. We are grateful to Danielle Mandikian and Matthew Case for useful comments on this manuscript.

The authors declare no competing financial interests.

Correspondence should be addressed to either of the following: Yugo Fukazawa, Division of Cerebral Structure, National Institute for Physiological Sciences, Okazaki 444-8787, Japan. E-mail: yugo@nips.ac.jp; or Akos Kulik, Department of Physiology II, University of Freiburg, D-79104 Freiburg, Germany. E-mail: Akos.Kulik@physiologie.uni-freiburg.de.

Y. Fukazawa's present address: Department of Anatomy and Molecular Cell Biology, Nagoya University Graduate School of Medicine, Nagoya 466-8550, Japan.

DOI:10.1523/JNEUROSCI.1142-12.2012

Copyright © 2012 the authors 0270-6474/12/3213555-13\$15.00/0

tencies in  $\text{Ca}_v2.3$  localization, a quantitative immunolabeling study with highly specific antibodies to  $\text{Ca}_v2.3$  is indispensable.

Previous calcium-imaging studies (Svoboda et al., 1996; Sabatini et al., 2002) have shown that dendritic shafts and spines operate in a functionally independent manner. It is reported that synaptic plasticity is variable among the spines (Matsuzaki et al., 2004) and calcium ions often exert their influence locally in neurons (for review, see Augustine et al., 2003). The existence of calcium microdomains suggests that calcium channels may not be distributed randomly and are more likely localized into defined membrane compartments. Hence, it is important to localize VGCC at a high spatial resolution by means of immunogold electron microscopy studies.

In this study, we generated specific antibodies against the RTCC  $\text{Ca}_v2.3$  subunit to study the regional distribution in mouse brain and to perform quantitative ultrastructural localization in the hippocampus. Apart from the predominant presynaptic expression in the interpeduncular nucleus (IPN),  $\text{Ca}_v2.3$  immunogold particles were mostly distributed postsynaptically in other regions. In dendritic spines of hippocampal pyramidal cells,  $\text{Ca}_v2.3$  immunogold particles were mainly observed in extrasynaptic plasma membrane, suggesting a preferential role of  $\text{Ca}_v2.3$   $\text{Ca}^{2+}$  signals in the activation of downstream molecules located in extrasynaptic sites. Furthermore, we demonstrate that the  $\text{Ca}_v2.3$  density in the spines does not correlate with that in the parent dendrites, supporting the view that spines are biochemical compartments that operate independently from their parent dendrites.

## Materials and Methods

**Animals.** In this study, 2-month-old female guinea pigs ( $n = 10$ ), 2–3-month-old adult male C57BL/6 mice ( $n = 10$ ), and age-matched, sex-matched  $\text{Ca}_v2.3$  knock-out (KO) mice ( $n = 7$ ) and postnatal day 20 rats ( $n = 2$ ) were used. Methodological details on the generation of  $\text{Ca}_v2.3$  KO mouse have been reported previously (Saegusa et al., 2000; Pervez et al., 2002). Animals were raised in a normal light/dark cycle in the authors' institutional animal facilities and were fed with food and water *ad libitum*. All the experiments were performed according to the institutional guidelines for animal welfare and the experimental protocol was approved by the animal care and use committees of the authors' institutions.

**Antibody production and Western blotting.** Guinea pig polyclonal  $\text{Ca}_v2.3$  antibodies against C-terminal sequence of mouse  $\text{Ca}_v2.3$  were generated using immunizing peptides directed against four different epitopes corresponding to the amino acid residues 2001–2017 (epitope 1), 2069–2087 (epitope 2), 2108–2127 (epitope 3), and 2231–2248 (epitope 4) of the mouse  $\text{Ca}_v2.3$  protein (Q61290, Fig. 1*F*). Each antigen (0.5 mg) or a mixture of four peptides (0.5 mg, referred to hereafter as pan-epitope antibody) was conjugated to 2 mg of keyhole limpet hemocyanin for immunization. Affinity purification of the sera was performed by using a mixed antigen peptide column (Aldevron). The pan-epitope and the epitope 2 antibodies were found to be suitable for immunohistochemistry.

Lysates from hippocampus and cortex of wild-type (WT) and age-matched  $\text{Ca}_v2.3$  KO mice were prepared by homogenization with a glass-Teflon homogenizer in RIPA buffer [50 mM Tris-HCl, pH 8.0, 150 mM NaCl, 1 mM EDTA, 1% (v/v) NP-40, 0.5% (w/v) sodium deoxycholate, 0.1% (w/v) SDS], including protease inhibitor mixture (Sigma-Aldrich) and 1 mM phenylmethylsulfonyl fluoride. Homogenates were centrifuged (14,000 relative centrifugal force, 15 min at 4°C) and the resulting supernatant was heated with loading buffer, including 20 mM DTT, at 37°C for 30 min. Fifty micrograms of each sample were subjected to SDS-PAGE and Western blotting according to standard procedures. Affinity-purified guinea pig polyclonal antibodies against the pan-epitope (1  $\mu\text{g}/\text{ml}$ ) or the  $\text{Ca}_v2.3$  epitope 2 (1  $\mu\text{g}/\text{ml}$ ) were used. After primary antibody incubation, sequential incubation with goat anti-guinea pig IgG-HRP (1:5000 dilution, Santa Cruz Biotechnology) was

performed. Immunoblots were visualized by enhanced chemiluminescence reagent captured on x-ray film.

**Tissue processing for light and electron microscopy.** Animal anesthetization, fixation, and tissue processing for light microscopy (LM) and pre-embedding immunoelectron microscopy (EM) were performed as described previously (Kulik et al., 2004; Parajuli et al., 2010). Deeply anesthetized animals were transcardially perfused through the ascending aorta with 25 mM PBS, pH 7.4, for 1 min. This was followed by a fixative containing 4% paraformaldehyde and 15% saturated picric acid made up in 0.1 M phosphate buffer (PB), pH 7.4, for 12 min at a flow rate of 5 ml/min. For electron microscopy, 0.05% glutaraldehyde was freshly added to the fixative solution. After perfusion, brains were quickly removed from the skull, washed briefly with PB, embedded in 1% agarose, and coronally sectioned at 50  $\mu\text{m}$  with a micro slicer (VT-1000, Leica).

Sections for LM analysis were rinsed several times in PBS, and then incubated in a blocking solution containing 10% normal goat serum (NGS, Vector Laboratories) and 0.1% Triton X-100 in PBS for 45 min. Sections were incubated overnight at 4°C with an affinity-purified polyclonal antibody against  $\text{Ca}_v2.3$  (1–2  $\mu\text{g}/\text{ml}$ ), made up in PBS containing 2% NGS and 0.1% Triton X-100, and were then washed in PBS and incubated with biotinylated goat anti-guinea pig IgG antibody (1:200, Vector Laboratories) at room temperature for 1 h. The sections were washed in PBS, and reacted with an avidin-biotinylated horseradish peroxidase complex (1:100 ABC-Elite, Vector Laboratories) made up in PBS containing 0.1% Triton X-100. After three washes in PBS and one in 50 mM Tris-HCl buffer (TB), pH 7.4, the peroxidase activity was visualized by incubating sections in TB containing 0.025% 3,3'-diaminobenzidine tetrahydrochloride (Dojindo Molecular Technologies) and 0.003% hydrogen peroxide. Sections were then transferred onto gelatin-coated glass slides and dehydrated through a graded series of ethanol, followed by xylene, and finally mounted under glass coverslips. Photomicrographs of the coronal sections were captured using a BX50 microscope equipped with a DP70 digital camera (Olympus).

For immunogold EM labeling, 50- $\mu\text{m}$ -thick cryoprotected sections were freeze-thawed. Subsequently, sections were blocked for 45 min in 20% NGS in Tris-buffered saline (TBS) and incubated overnight at 4°C in primary antibody (1–2  $\mu\text{g}/\text{ml}$ ) made up in TBS, pH 7.4, containing 1% NGS. After washing, the sections were incubated with 0.8 nm gold-coupled (Aurion) or 1.4 nm gold-coupled (Nanoprobes) anti-guinea pig secondary antibodies diluted in TBS at a ratio of 1:100. After washing, the sections were postfixed in 1% glutaraldehyde for 10 min, followed by silver enhancement of the immunogold particles using either an Aurion R-gent SE (Aurion) or a HQ silver (Nanoprobes) EM intensification kit. Sections were then postfixed with 1% osmium tetroxide for 30–40 min, *en bloc* counterstained with 1% uranyl acetate for 30 min, and dehydrated in graded ethanol series followed by propylene oxide. The sections were infiltrated overnight at room temperature in Durcupan resin (Sigma-Aldrich) and transferred to glass slides for flat embedding. After resin curing at 60°C, the trimmed tissues from the region of interest were re-embedded in Durcupan resin blocks for ultrathin sectioning. Serial 70-nm-thick sections were cut from the surface (within 3  $\mu\text{m}$  depth) of the samples and were collected in pioloform-coated single-slot copper grids. Images were captured with a CCD camera connected to a Philips EM208S transmission electron microscope.

**Identification of profiles.** The neuronal elements in the CA1 area can be differentiated from glial cells based on morphological criteria. Glial processes often have highly irregular shapes and possess a pale cytoplasmic mass that contains many prominent dark glycogen granules and parallel bundles of intermediate filaments (Peters et al., 1991). A profile was judged as being a presynaptic terminal if its characteristics included synaptic vesicle accumulation, presence of presynaptic specializations, and rigid alignment of presynaptic membrane to its postsynaptic partner. Synapses were identified based on postsynaptic thickening and electron dense materials in the synaptic cleft (Peters et al., 1991). Pyramidal cell dendrites had symmetrical shaft synapses and asymmetrical synapses on spine heads with narrow, cylindrical neck-like structures (for review, see Bourne and Harris, 2008). These spiny protrusions did not contain any mitochondria. Dendritic profiles lacking spiny protrusions and possess-

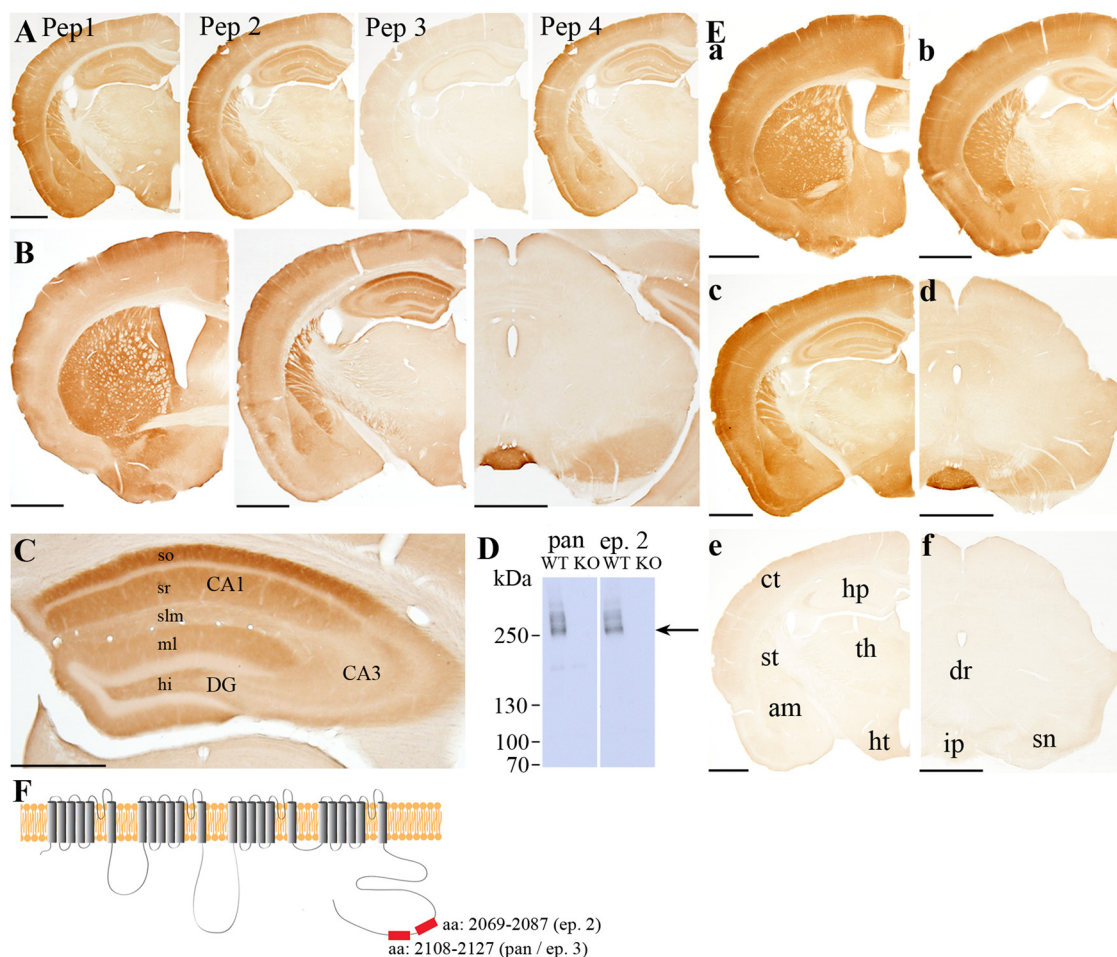


**Figure 1.** Ubiquitous expression of  $\text{Ca}_v2.3$  in the mouse brain. **A**, Preincubation of  $\text{Ca}_v2.3$  pan-epitope antibody with the epitope 3 peptide abolished  $\text{Ca}_v2.3$  immunoreactivity. Note that the pattern and immunostaining intensity were not changed in those sections stained by the pan-epitope antibody preincubated with antigenic peptides against epitopes 1, 2, or 4. **B**, Brain sections reacted with the epitope 2 antibody displayed strong immunoreactivity in the cortex, hippocampus, striatum, amygdala, and the interpeduncular nucleus. **C**, A high-magnification image of hippocampus showing stronger immunoreactivity for  $\text{Ca}_v2.3$ , obtained using the epitope 2 antibody, in the stratum oriens (so) and stratum radiatum (sr) than in the stratum lacunosum moleculare (slm) of the CA1 area. Note that the immunoreactivity in the CA3 area is weaker than in the corresponding area of the CA1. In the dentate gyrus (DG), the molecular layer (ml) and the hilar region (hi) show moderate immunoreactivity. **D**, Western blot analysis of hippocampal and cortical lysates from WT and  $\text{Ca}_v2.3$  KO mouse brains by using the pan-epitope and epitope 2 antibodies. The band at 250 kDa (arrow, predicted molecular weight of  $\text{Ca}_v2.3$ ) (Soong et al., 1993) was present only in the WT preparation, not in the KO. **E**, Light microscopic images of mouse brain sections stained with the  $\text{Ca}_v2.3$  pan-epitope antibody. Staining was observed throughout the rostrocaudal extent of the brain. Particularly strong immunoreactivity for  $\text{Ca}_v2.3$  was seen in the superficial layer of the cortex, hippocampus, striatum, amygdala, and the interpeduncular nucleus. Immunoreactivity seen in the WT (**a–d**) brain was not visible in the  $\text{Ca}_v2.3$  KO brain (**e** and **f**). **F**, Transmembrane topology of the  $\text{Ca}_v2.3$ , a subunit showing the location of the amino acid residues (red rectangle) recognized by epitope 2 (ep. 2) and pan-epitope (pan/ep. 3) antibodies used in this study. aa, amino acids; am, amygdala; ct, cortex; dr, dorsal raphe nucleus; hp, hippocampus; ht, hypothalamus; ip, interpeduncular nucleus; sn, substantia nigra; st, striatum; th, thalamus. Scale bars, 500  $\mu\text{m}$ .

ing numerous asymmetrical synapses on their shafts were identified as interneurons (Megias et al., 2001) and were omitted from the analysis.

**Quantification of LM immunoreactivity.** To obtain quantitative measure of LM immunoreactivity for  $\text{Ca}_v2.3$ , all images of WT and  $\text{Ca}_v2.3$  KO brain sections were acquired under the same microscopic settings. Images were then uploaded to NIH ImageJ software, converted to 8 bit grayscale and inverted. Densitometric measurements were performed at three different areas within individual regions of interest using the mean intensity measurement function of the software. Average background levels were determined by quantification from many areas in the KO brain. All WT measurements were corrected using the established KO baseline. These values were used to group nuclei into five expression categories as listed in Table 1.

The epitope 2 antibody was chosen for LM mapping because the pan-epitope antibody showed some nonspecific staining in the stratum lucidum of the hippocampal CA3 area, cerebellum, and inferior olive in the  $\text{Ca}_v2.3$  KO tissues.

**Immunogold quantification.** Serially sectioned images were imported into the Reconstruct software (Fiala, 2005) and the image stacks were aligned. Plasma membranes of individual dendrites and spine heads were

manually traced. To obtain a spine head volume, the total cross-sectional area of the closed contours, formed by manually delineating the head of a given complete spine, was multiplied by the section thickness (70 nm). The surface area was estimated as a product of the section thickness and effective plasma membrane length. The length of the imaginary line introduced at the plasma membrane discontinuity portion in the head-neck junction, while drawing the closed contours, was measured using the trace tool function. This length was subtracted from the length of the closed contours to obtain an effective plasma membrane length. Dendritic diameter was obtained as an average of distance connecting the shortest elliptical axis of a given dendrite in each of the serial images. The calculated volume and surface area of neuronal profiles were not corrected for tissue shrinkage that may occur during dehydration steps (Trommald et al., 1995).

To introduce uniformity for counting silver-intensified immunogold particles, we applied stringent and constant measures. The average diameter of immunogold particles was  $\sim 20$ – $25$  nm. If a single immunogold particle was cut into two during ultrathin sectioning, this could lead to the visualization of two immunogold particles appearing in two consecutive sections. To avoid overestimating, immunogold particles were



**Table 1. Intensity of immunoreactivity for Ca<sub>v</sub>2.3 subunit in various brain regions obtained with the epitope 2 antibody**

Area	Intensity in arbitrary unit	Category
Olfactory		
Main olfactory bulb	15 ± 0.6	Low
Accessory olfactory bulb	13 ± 4.4	Low
Anterior olfactory nucleus	18 ± 1.1	Low
Olfactory tubercle	45 ± 6.3	High
Cerebral neocortex (somatosensory cortex)		
Layer 1–3	45 ± 1.8	High
Layer 4–6	20 ± 1.4	Intermediate
Amygdala		
Central amygdaloid nucleus	44 ± 1.6	High
Lateral amygdaloid nucleus	20 ± 0.8	Intermediate
Basolateral amygdaloid nucleus	36 ± 0.4	High
Basal ganglia		
Bed nucleus of stria terminalis	6 ± 0.9	Low
Caudate putamen (striatum)	51 ± 3.2	Very high
Accumbens nucleus (core)	43 ± 2.1	High
Accumbens nucleus (shell)	10 ± 0.2	Low
Globus pallidus	48 ± 2.2	High
Substantia nigra	24 ± 1.5	Intermediate
Ventral tegmental area	−3 ± 0.8	Negative
Subthalamic nucleus	3 ± 2.2	Negative
Hippocampus		
CA1		
Stratum launosum moleculare	19 ± 1.2	Intermediate
Stratum radiatum	45 ± 0.8	High
Stratum pyramidale	N.A.	
Stratum oriens	65 ± 2.1	Very high
CA3		
Stratum lacunosum moleculare	16 ± 0.4	Low
Stratum radiatum	8 ± 0.5	Low
Stratum lucidum	14 ± 0.3	Low
Stratum pyramidale	N.A.	
Stratum oriens	18 ± 0.8	Low
Dentate gyrus		
Molecular layer	27 ± 0.1	Intermediate
Granule cell layer	N.A.	
Hilus	24 ± 0.4	Intermediate
Septum (Lateral)	24 ± 0.7	Intermediate
Thalamus		
Lateral geniculate nucleus	−7 ± 0.7	Negative
Medial Geniculate nucleus	13 ± 0.5	Low
Reticular nucleus	−1 ± 0.7	Negative
Epithalamus		
Medial Habenula	0 ± 1.2	Negative
Lateral Habenula	−1 ± 1.1	Negative
Hypothalamus	24 ± 0.1	Intermediate
Reticular core		
Periaqueductal gray	−6 ± 0.8	Negative
Ventral tegmental area	−3 ± 0.8	Negative
Raphe nucleus	−10 ± 0.5	Negative
Interpeduncular nucleus	60 ± 4.5	Very high
Sensory brainstem area		
Cochlear nucleus	41 ± 0.6	High
Lateral superior olive	9 ± 0.5	Low
Medial nucleus of trapezoid body	2 ± 0.1	Negative
Superior colliculus	0 ± 1.0	Negative
Inferior colliculus	4 ± 0.8	Negative
Vestibular nucleus	2 ± 0.2	Negative
Cerebellum		
Molecular layer	5 ± 0.7	Low
Purkinje cell layer	N.A.	
Granule cell layer	32 ± 0.6	Intermediate

Table continues

**Table 1. Continued**

Area	Intensity in arbitrary unit	Category
Precerebellar and postcerebellar nuclei		
Pontine nuclei	5 ± 0.6	Low
Inferior olive	10 ± 3.7	Low

Intensity of immunoreactivity for Ca<sub>v</sub>2.3 obtained by the epitope 2 antibody was quantified in individual brain areas. See Materials and Methods for details of the quantification. Values are expressed as mean ± SEM. Areas with significant immunosignals and related areas were shown in this table. Those immunonegative for Ca<sub>v</sub>2.3 were not listed. Nuclei were grouped into 5 expression categories based on the intensity. Ranges of each category are as follows: negative, <5; low, 5–<20; intermediate, 20–<35; high, 35–<50; very high, ≥50. N.A., not analyzed.

counted as one if two immunogold particles appeared exactly at the same location in two consecutive sections. However, in such a case, we introduced a criterion that the diameter of one of the immunogold particles should be half or less than the average diameter of the silver-intensified immunogold particles in the surrounding profiles.

Immunogold quantification on serial electron microscopic images was made using two adult WT mice, one postnatal day 20 rat, and one adult Ca<sub>v</sub>2.3 KO mouse. Conclusions drawn from the quantification were further confirmed in five more WT mice at the qualitative level. To establish a baseline for background labeling, multiple serial sections were reconstructed from hippocampal CA1 and immunogold particles were counted in both WT and Ca<sub>v</sub>2.3 KO brains from 334 μm<sup>2</sup> area of each. Quantification of immunogold particles in the hippocampus was performed with the pan antibody, rather than epitope 2, as the former gave stronger labeling in our experimental condition.

The chain lengths of the primary and secondary antibodies inherently constrain the spatial resolution of the immunogold labeling method. Thus, it is inevitable to see individual immunogold particles located at a slight distance away from the exact site of the antigen (Matsubara et al., 1996). To confirm the membrane origin of Ca<sub>v</sub>2.3 labeling, we measured the perpendicular distances between the center of the individual gold particles ( $n = 238$ ) and the center of nearest membranous structure. The measured distances were allocated to a bin width of 5 nm and the frequency of immunogold particles in each bin was counted (data not shown). The histogram distribution gave a single peak between 15 and 20 nm (median, 16.24 nm; mean, 17.70 nm; SD, 12.26 nm) and a long tail toward higher values. Approximately 95% of the immunogold particles were found to be located within 42 nm (mean + 2 × SD) of the cytoplasmic face of the membrane, and this distance was taken as the threshold for considering immunogold particles as being attached to the plasma membrane. This threshold distance is consistent with reports from earlier studies (Lörincz et al., 2002; Báldi et al., 2010; Parajuli et al., 2010).

The distance of immunogold particles measured from the nearest edge of the PSD was expressed as a negative value if particles were located along the plasma membrane within the main body of the PSD, and as a positive value if immunogold particles were seen on the extrasynaptic plasma membrane. Higher positive values represent immunoparticles farther away from the edge of the PSD.

Statistical analysis was conducted using SPSS (SPSS) and the level for statistical significance was set at 0.05. Normality of the data was assessed by applying Shapiro–Wilk's  $W$  test. Statistical evaluation of immunogold densities was performed with the Student's  $t$  test, Mann–Whitney  $U$  test, or one-way ANOVA where appropriate. Correlation was examined by Spearman's rank order test. All results are reported as mean ± SEM.

## Results

### Epitopes recognized by Ca<sub>v</sub>2.3 antibodies

To identify the epitope(s) recognized by the pan-epitope antibody, each of the four antigenic peptides against Ca<sub>v</sub>2.3 were separately incubated at a 10-fold excess in concentration with the antibody for 30 min. The resulting adsorbed antibody was applied to the sections for LM immunohistochemistry. While sections immunostained by the pan-epitope antibody preadsorbed with antigenic peptides against epitope 1, 2, or 4 resulted in signal

indistinguishable from the control sections (sections stained by the pan-epitope antibody alone), peptide 3-adsorbed pan-epitope antibody showed no clear immunostaining (Fig. 1A). Thus, these results clearly demonstrate that specific signal generated by the pan-epitope antibody is attributable to the recognition of epitope 3 region (amino acid residues: 2108–2127) of  $\text{Ca}_v2.3$  (Fig. 1F).

We also generated antibodies against each of the four epitopes, and determined their suitability for immunohistochemistry. Antibodies against epitopes 1, 3, or 4 did not produce any specific staining for  $\text{Ca}_v2.3$  (data not shown). However, the antibody against epitope 2 (amino acid residues: 2069–2087) gave a staining pattern (Fig. 1B,C) similar to that obtained by the pan-epitope antibody (Fig. 1Ea–d), which provides additional evidence for the specificity of our antibodies to  $\text{Ca}_v2.3$ .

### Light microscopic immunohistochemistry and Western blotting for $\text{Ca}_v2.3$

Immunohistochemistry revealed that  $\text{Ca}_v2.3$  was distributed ubiquitously throughout the brain at varying intensities among different regions as summarized in Table 1. The staining was more prominent in the forebrain compared with the midbrain and hindbrain. Neuropils of the olfactory tubercle, superficial layers of the cortex, hippocampus, lateral septum, striatum, nucleus accumbens, IPN, and the central and basolateral amygdala showed more intense staining (Fig. 1B, Ea–d), whereas the staining intensity was moderate in such areas as the hypothalamus and substantia nigra. The immunoreactivity in the thalamus, ventral tegmental area, and raphe nucleus was low or close to background levels. The immunohistochemical distribution of  $\text{Ca}_v2.3$  correlates very well with previously published *in situ* hybridization results (Soong et al., 1993; Williams et al., 1994; Lein et al., 2007) except for some regions, such as the medial habenula, IPN, and the dorsal raphe nucleus. The *in situ* data show  $\text{Ca}_v2.3$  mRNA in the medial habenula, with no transcript in the IPN, which is opposite to the  $\text{Ca}_v2.3$  immunoreactivity pattern observed in our study. It is interesting to note that neurons in the medial habenula primarily project to the IPN and thus presynaptic targeting of  $\text{Ca}_v2.3$  in this locus can be inferred.

A remarkable difference in the intensity of immunoreactivity was seen between the CA1 and CA3 areas (Fig. 1C) of the hippocampus. In sharp contrast to the strong  $\text{Ca}_v2.3$  immunoreactivity in the CA1 area, only a faint immunostaining could be observed in dendritic layers of the CA3 area. The distribution of immunoreactivity for  $\text{Ca}_v2.3$  subunit in the CA3 field was not homogenous throughout the dendritic extent but rather enriched in the stratum oriens (SO) and stratum lucidum. In the CA1 area, the neuropil in the SO displayed stronger immunoreactivity than the neuropil in the proximal part of the stratum radiatum (PSR) and stratum lacunosum moleculare. In the dentate gyrus, the staining intensity was similar throughout the molecular layer. The immunoreactivity in somata of granule cells was barely detected. The pattern and intensity of immunoreactivity detected in the hippocampus and other brain regions in WT sections (Fig. 1A–C, Ea–d) disappeared in tissues obtained from  $\text{Ca}_v2.3$  KO animals (Fig. 1Ee,f). However, in the stratum lucidum, a faint immunoreactivity was still evident in  $\text{Ca}_v2.3$  KO sections using the pan-epitope antibody, but not the epitope 2 antibody. This was likely due to the cross reactivity of the pan-epitope antibody with other protein(s) in this region.

The specificity of the pan-epitope antibody and the epitope 2 antibody was further confirmed by Western blot analysis of hippocampal and cortical lysates made from both WT and  $\text{Ca}_v2.3$

KO mice. A 250 kDa band corresponding to the predicted molecular weight of  $\text{Ca}_v2.3$  (Soong et al., 1993) disappeared in the KO lysate (Fig. 1D).

### General description of the electron microscopic localization of immunogold particles

The ultrastructural localization of  $\text{Ca}_v2.3$  was performed using the pre-embedding immunogold labeling methods. Both pan-epitope and epitope 2 antibodies produced identical patterns of immunostaining in the brain regions examined. Images were taken from the CA1, cortex, and the amygdala using the pan-epitope antibody, and from the striatum, CA3 stratum lucidum, and the IPN using the epitope 2 antibody.

As expected from the intracellular location of the epitopes recognized by the  $\text{Ca}_v2.3$  antibodies, immunoparticles were localized intracellularly along the plasma membranes of both postsynaptic and presynaptic elements (Figs. 2–4; see Fig. 7). Cytosolic labeling was sparse, but if present the immunogold particles were often observed in the vicinity of some intracellular membranous structures (data not shown). Immunogold particles along the plasma membrane were observed either as a discrete individual particle (Figs. 2–4; see Fig. 7) or as clusters of two (for instance, Fig. 2C with epitope 2 antibody or Fig. 4D with pan-epitope antibody).

The EM immunogold analysis in the hippocampus, neocortex, striatum, and amygdala revealed that the channel subunit is preferentially localized postsynaptically in dendritic shafts and spines and, to a lesser extent, in presynaptic compartments. Particles were diffusely distributed along the plasma membrane of dendrites and the spines without any preference to specialized membrane compartments (e.g., postsynaptic density, apposition to glial contact, etc.). In the CA3 stratum lucidum, the immunogold particles were seen in the CA3 pyramidal cell dendrites, thorny excrescence spines, and the mossy fiber terminals (Fig. 2D–F). In the mossy fiber terminals, particles could be seen both in the active zone (AZ) of the terminals (Fig. 2E) or remote from the presynaptic membrane specialization (Fig. 2F).

In contrast to the strong postsynaptic labeling in the other brain areas, immunogold particles were densely localized in the presynaptic boutons of the medial habenula (MHb) terminals in the IPN (Fig. 2G–K). Labeling was observed both in the crest (Fig. 2G, arrows) and *en passant* S synapses (Fig. 2J,K), both of which in the IPN are shown to be derived from MHb fibers (Lenn, 1976).  $\text{Ca}_v2.3$  immunogold particles were observed primarily in the extrasynaptic plasma membrane and occasionally over the presynaptic AZ, indicating a distinct distribution pattern compared with  $\text{Ca}_v2.1$  channels (Kulik et al., 2004; Holderith et al., 2012).

The strong immunoreactivity seen in the WT sections (Figs. 2–4; see Fig. 7) was largely absent in the  $\text{Ca}_v2.3$  KO sections (Fig. 4G). To quantitatively estimate the background labeling produced by the pan-epitope antibody, we counted the total number of immunogold particles observed in the  $334 \mu\text{m}^2$  area in the CA1 radiatum in both WT and  $\text{Ca}_v2.3$  KO sections. We counted a total of 540 immunogold particles in WT and 15 in KO in the postsynaptic compartments (dendrites and spines) and 216 immunogold particles in WT and 51 in KO in the presynaptic compartments.

### $\text{Ca}_v2.3$ channels are mostly postsynaptic in CA1 region

In the CA1 of the hippocampus, immunogold labeling was observed postsynaptically in the somata, dendritic shafts, and spines of the putative pyramidal cells (Figs. 3A–D, 4A, C–F). In the PSR,



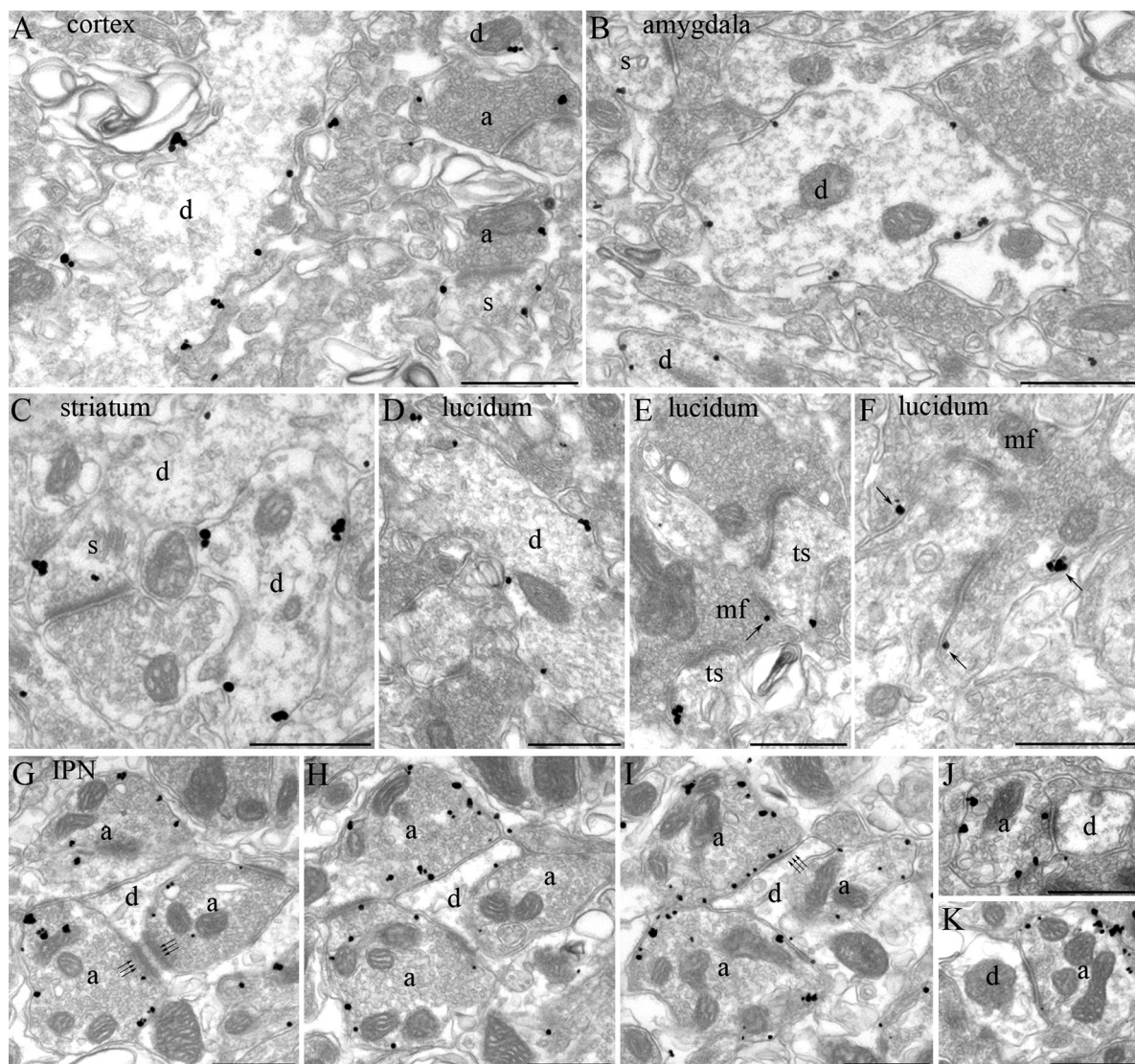


**Figure 2.** Distinct presynaptic or postsynaptic localization patterns of  $\text{Ca}_v2.3$  among the brain regions. **A–C**, Electron micrographs showing immunogold particles for  $\text{Ca}_v2.3$  in layer 2/3 of the somatosensory cortex (**A**), amygdala (**B**), and striatum (**C**). Most of the particles in these regions are observed in the dendrites (d) and spines (s). **D–F**, Immunogold particles are localized to the dendrites (d), thorny excrescence spines (ts), and mossy fiber boutons (mf) in the CA3 stratum lucidum. In the mossy fiber boutons, the immunoparticles can be seen directly over the active zone (**E**, arrow) or at extrasynaptic plasma membrane of boutons remote from the active zone (**F**, arrows). **G–K**, Strong immunolabeling for  $\text{Ca}_v2.3$  is observed in the presynaptic terminals in the interpeduncular nucleus (IPN). Crest synapse boutons (**G–I**) and *en passant* boutons (**J, K**) are both positive for  $\text{Ca}_v2.3$ . Arrows show the typical morphology of a crest synapse. Images **G–I** are series images of the same bouton. Images **C–K** obtained by using the epitope 2 antibody. a, axon terminal. Scale bars, 500 nm.

the big-caliber (Fig. 4E) and the small-caliber (Fig. 4A) dendrites were both immunopositive for  $\text{Ca}_v2.3$ . In the presynaptic compartments,  $\text{Ca}_v2.3$  labeling was detected at the extrasynaptic plasma membrane (Figs. 3C,E, 4B,D), and over the presynaptic AZ (Fig. 3A,D). Particles were also seen in the inhibitory boutons terminating on pyramidal cell dendrites (Figs. 3C, 4B). In some cases, a presynaptic terminal and its postsynaptic spine were both seen to be positive for  $\text{Ca}_v2.3$  (Figs. 3A,D, 4D). Plasma membranes of myelinated axons were also positive for  $\text{Ca}_v2.3$  (Fig. 3F). In contrast to neuronal elements, glial cells showed no immunoreactivity for the protein.

The predominant postsynaptic localization of  $\text{Ca}_v2.3$  subunit in the SO and PSR was clearly apparent from the qualitative analysis of the immunogold particle distribution. To provide a numerical comparison of the immunogold particles between the postsynaptic and presynaptic compartments, quantitative analysis was performed using ~25 serial sections obtained from PSR

(within 100  $\mu\text{m}$  from the soma). Of the 4122 plasma membrane-bound particles counted, 3225 (78.2%) were observed in the postsynaptic compartments (dendritic shafts and spines) and 897 (21.8%) in the presynaptic compartments. Postsynaptically, 1967 (47.7%) particles were observed in the dendritic shafts and 1258 (30.5%) in the spines. In the presynaptic compartment, 29 (0.7%) particles were observed in the AZ and 868 (21.1%) particles were seen in the rest of the presynaptic plasma membrane. This quantitative data obtained from PSR further strengthens our qualitative observations regarding predominant postsynaptic localization of  $\text{Ca}_v2.3$  in the CA1.

#### Quantification of the relative channel density between dendritic shafts, spine heads, and somata

The subcellular distribution of ion channels at the neuronal plasma membrane can be highly regulated and complex. Ion channels can either be distributed uniformly or be selectively



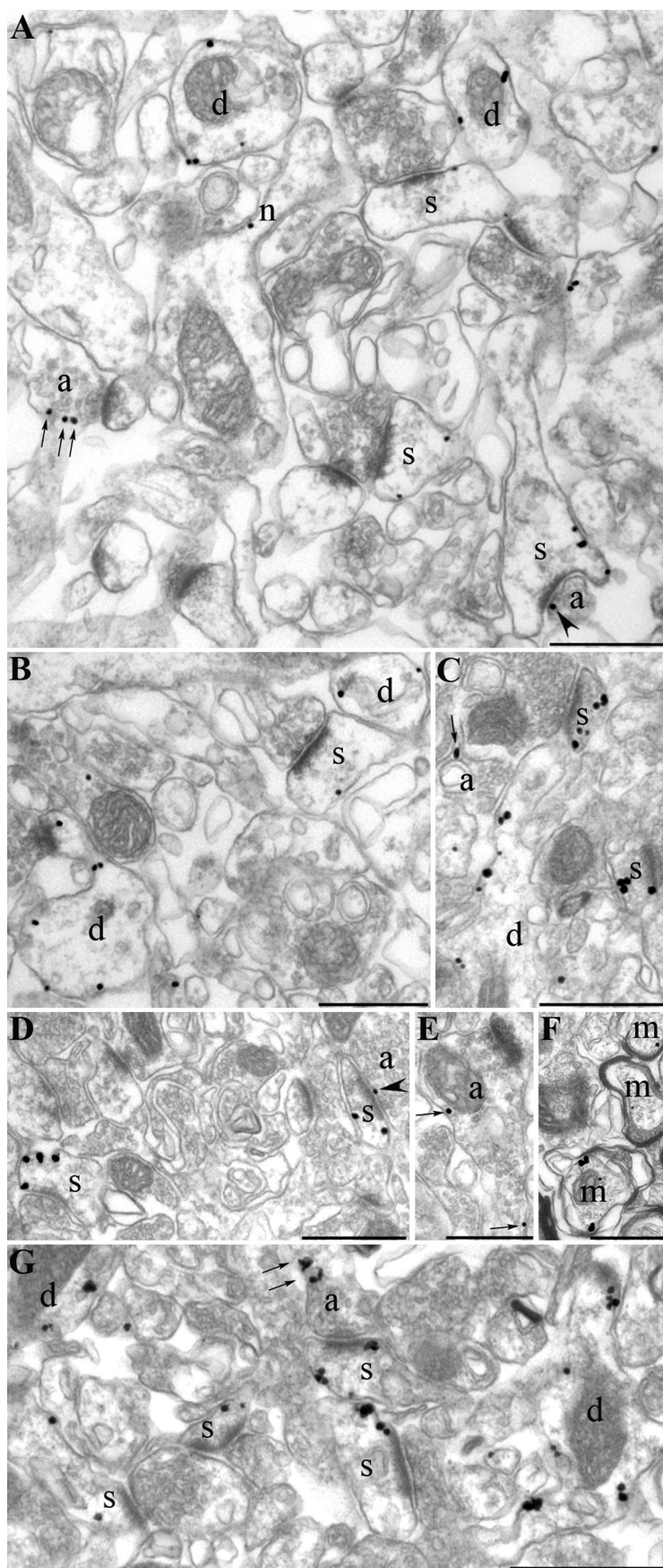


**Figure 3.**  $\text{Ca}_v2.3$  proteins are localized to both presynaptic and postsynaptic compartments in the SO of CA1. **A–F**, Ultrastructural localization of immunogold particles for  $\text{Ca}_v2.3$  in the SO were revealed by pre-embedding immunogold labeling

targeted to a specific neuronal compartment at a significantly higher density (for review, see Nusser, 2009). To examine whether  $\text{Ca}_v2.3$  shows uniform or compartmentalized distribution, dendritic spine heads, shafts, and somata of pyramidal cells were investigated in 15–30 serial ultrathin sections and the average immunogold particle densities in each of these domains were calculated (Fig. 5A). Completely reconstructed spines, whose heads could be clearly distinguished from their necks, were included in the analysis.

From a total of 19 dendritic shafts and 119 spine heads studied in the SO, the average immunogold particle density was  $8.7 \pm 0.52$  particles/ $\mu\text{m}^2$  (median, 8.2 particles/ $\mu\text{m}^2$ ; range, 5.3–14.5 particles/ $\mu\text{m}^2$ ) and  $9.2 \pm 0.65$  particles/ $\mu\text{m}^2$  (median, 8.2 particles/ $\mu\text{m}^2$ ; range, 0–30.6 particles/ $\mu\text{m}^2$ ), respectively ( $p = 0.80$ , Mann–Whitney  $U$  test). In the PSR, 30 dendritic shafts and 154 spines were analyzed. The average immunogold particle density was  $9.4 \pm 0.49$  particles/ $\mu\text{m}^2$  (median, 9.0 particles/ $\mu\text{m}^2$ ; range, 5.4–16.7 particles/ $\mu\text{m}^2$ ) in the dendritic shafts and  $8.6 \pm 0.63$  particles/ $\mu\text{m}^2$  (median, 7.8 particles/ $\mu\text{m}^2$ ; range, 0–40.4 particles/ $\mu\text{m}^2$ ) in the spine heads ( $p = 0.17$ , Mann–Whitney  $U$  test, Fig. 5A). When the average immunogold particle density was compared across the strata, no statistical difference could be revealed either between the dendrites ( $p = 0.37$ , Student's  $t$  test) or between the spines ( $p = 0.33$ , Mann–Whitney  $U$  test). Interestingly, much higher variability of  $\text{Ca}_v2.3$  density was observed in spines than in the dendritic shafts [coefficient of variation (CV) in spines: SO, 0.78; PSR, 0.91. CV in dendrites: SO, 0.26; PSR, 0.29].

To obtain information about the abundance of RTCC in the pyramidal cell somata, the immunogold particle density was calculated from the partially reconstructed pyramidal cell somata ( $n = 6$ ). An average immunogold particle density of  $5.3 \pm 0.57$  particles/ $\mu\text{m}^2$  (median, 5.7

method using the pan-epitope antibody. Immunoparticles were observed along the plasma membrane of dendritic shafts (d), spine head (s), spine neck (n), and axon terminals (a). Immunogolds are more evident in the postsynaptic site. Particles in the presynaptic compartments were seen either over the active zone (A and D, arrowheads) or at the extrasynaptic plasma membrane of boutons remote from release sites (A, C, and E, arrows). Myelinated axons (m) were also positive for  $\text{Ca}_v2.3$  (F). G, Immunogold particles for  $\text{Ca}_v2.3$  are seen predominantly in the postsynaptic compartments in SO of the postnatal day 20 rat. Arrows show presynaptic immunogold particles. Scale bars, 500 nm.



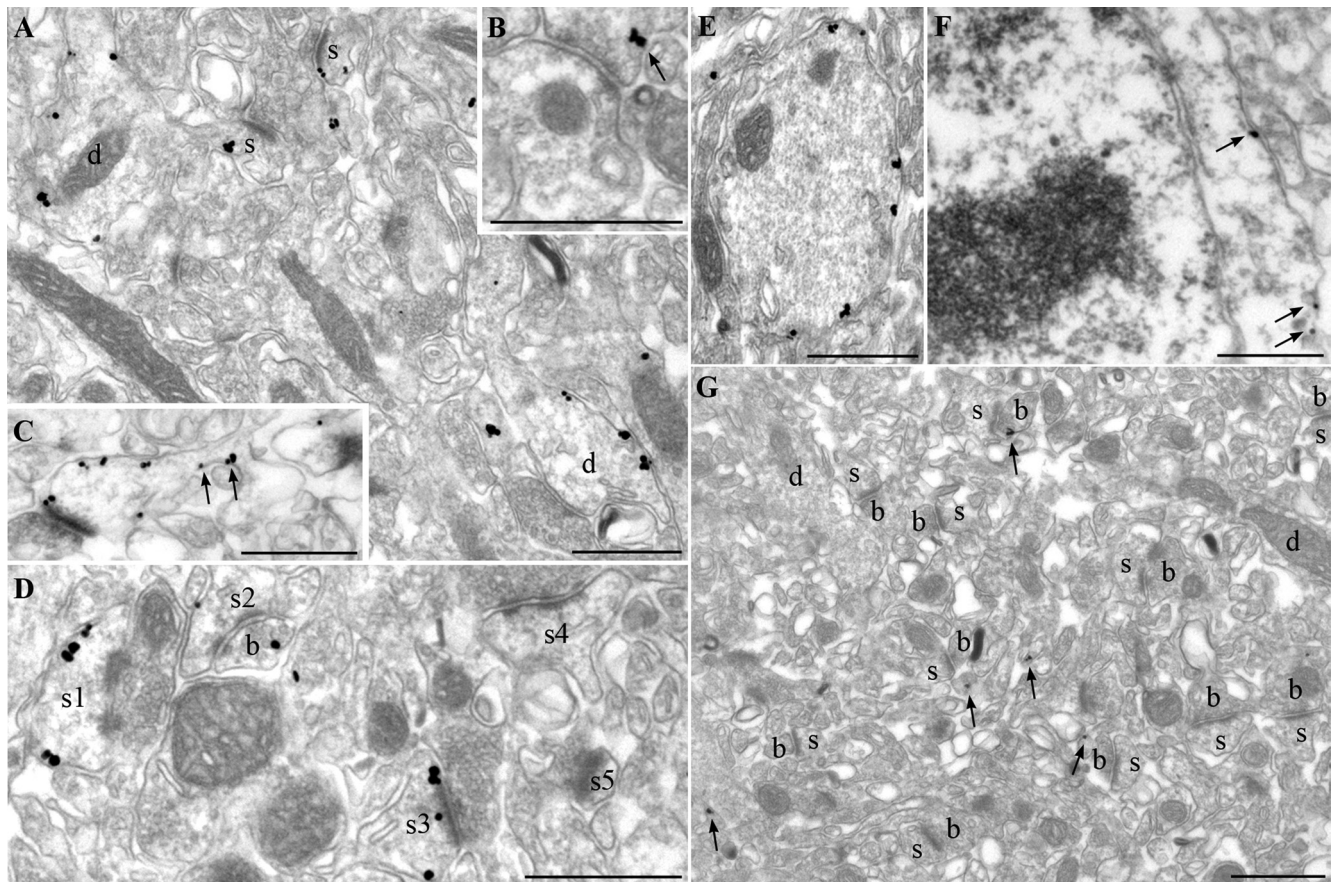


**Figure 4.**  $\text{Ca}_v2.3$  proteins are localized to both presynaptic and postsynaptic compartments in the PSR of the CA1. Electron micrographs showing immunogold particles for  $\text{Ca}_v2.3$  in CA1 PSR using the pan-epitope antibody. **A–E**, Immunogold particles are localized to the plasma membrane of dendritic shafts (d), spines (s), and presynaptic boutons (b). Particles in the presynaptic compartments were seen in the putative excitatory (**D**, b) as well as the inhibitory (**B**) terminals. In the dendritic domains, immunogold particles were seen both in the small-caliber (**A**, d) as well as in big-caliber (**E**) dendrite. **C**, Immunogold particles are localized in the plasma membrane of the spine neck (arrows) as well as the spine head. **D**, The immunolabeling intensity varied among the similarly sized dendritic spines. Spine (S1) is strongly labeled. Spines S2 and S3 are moderately labeled and S4 and S5 are immunonegative. **F**, Somatic plasma membranes are also immunopositive for  $\text{Ca}_v2.3$ . **G**, An electron micrograph taken from the  $\text{Ca}_v2.3$  KO sections reacted with the pan-epitope antibody. No immunogold particle could be seen in the dendrites (d) and spines (s) in the  $\text{Ca}_v2.3$  KO sections. Although most of the presynaptic immunolabeling disappeared in the KO sections, some axons and presynaptic boutons (b) still displayed 1–2 immunogold particles (arrows). Scale bars, 500 nm.

particles/ $\mu\text{m}^2$ ; range, 3.0–6.6 particles/ $\mu\text{m}^2$ ) was obtained in this compartment, which was significantly lower than that of dendrites in SO and PSR ( $p < 0.01$ , one-way ANOVA).

#### Immunogold density in primary apical dendrites and oblique dendrites

There is an increasing interest regarding the difference in ion channel density between the primary apical dendrites and their oblique branches. These two dendritic segments differ in their diameter and thus in the surface-to-volume ratio. In addition, the CA1 oblique dendrites harbor most of the spines and may therefore receive stronger excitatory inputs when compared with the primary apical dendrites (Megias et al., 2001; Frick et al., 2003). Thus, it would be informative to compare the expression density of calcium channels between these two dendritic compartments. However, partly because dendritic patch recordings are still inaccessible to the small oblique branches, data bearing on the issues of relative channel density and the possible differences in the signal processing mechanisms between primary apical dendrites and their oblique branches are largely lacking. Due to the technical advantage of EM methods in studying channel distribution, we were able to explore how  $\text{Ca}_v2.3$  density compares between primary apical and oblique dendrites. When we measured the dendritic diameters of individual dendritic shafts in PSR, we found that the dendrites could be classified into two

groups (Fig. 5B). One group had a dendritic diameter ranging from 0.58 to 1.12  $\mu\text{m}$  ( $n = 7$ ) and the other group had a dendritic diameter ranging from 0.21 to 0.36  $\mu\text{m}$  ( $n = 23$ ). These two groups putatively represent primary apical dendrites and oblique dendrites, respectively. The average labeling density in the primary apical dendrites was  $8.3 \pm 0.61$  particles/ $\mu\text{m}^2$  (median, 8.0 particles/ $\mu\text{m}^2$ ; range, 6.6–11.5 particles/ $\mu\text{m}^2$ ) and in oblique dendrite was  $9.7 \pm 0.61$  particles/ $\mu\text{m}^2$  (median, 9.5 particles/ $\mu\text{m}^2$ ; range, 5.4–16.7 particles/ $\mu\text{m}^2$ ). When the average labeling density was compared between these two dendritic populations, no significant difference could be detected ( $p = 0.25$ , Student's *t* test), suggesting that oblique dendrites realize higher intracellular calcium rises than primary apical dendrites upon depolarization. It is also important to note that there was a larger variability in oblique than primary apical dendrites (CV, 0.30 and 0.19 for oblique and primary apical dendrites, respectively) in the labeling density among individual dendrites. Such variability may suggest that each segment of oblique dendrites acts as a functional unit with distinct calcium dynamics and excitability.

#### Proportion of immunogold particles between spine head and spine neck

A previous study of Bloodgood and Sabatini (2007) using two-photon calcium imaging has reported that  $\text{Ca}_v2.3$  channels are localized in the spine heads, but not in the spine necks. However,



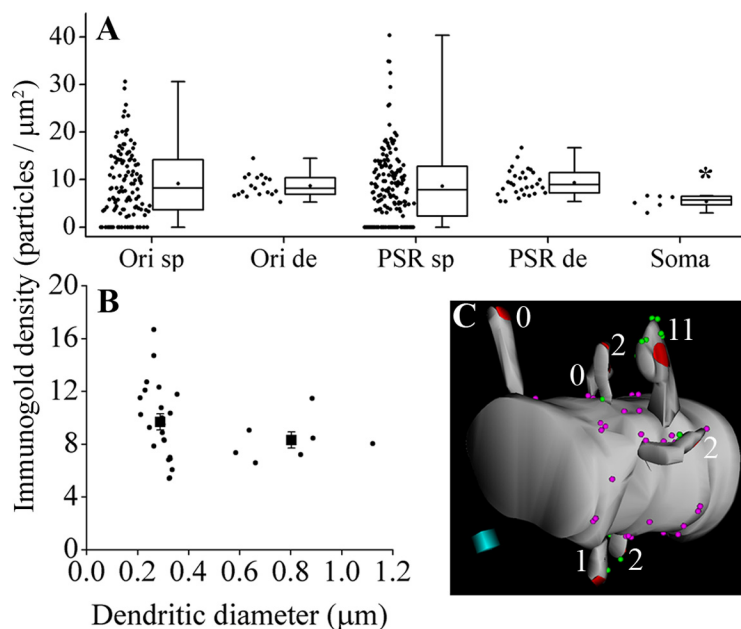


**Figure 5.** Somatodendritic compartmentalization of  $\text{Ca}_v2.3$  in the CA1. **A**, The density of immunolabeling for  $\text{Ca}_v2.3$  in various neuronal compartments is plotted two ways: a dot plot of individual data points (left) and a box-and-whisker plot (right) demonstrating quartiles, median, maximum, and minimum of the data. Mean density is indicated with a dot. Quantification of  $\text{Ca}_v2.3$  immunoreactivity demonstrated a higher average density of the channel protein in dendritic shafts when compared with pyramidal cell somata ( $p < 0.01$  against dendrites in SO and PSR, one-way ANOVA). Note that even within the same neuronal compartment, the immunogold density is highly variable. The variability is the highest in spines, moderate in dendrites and lowest in the cell somata. Ori de, stratum oriens dendrites; Ori sp, stratum oriens spines; PSR de, proximal stratum radiatum dendrites; PSR sp, proximal stratum radiatum spines; Soma, Somata of CA1 pyramidal cells. **B**,  $\text{Ca}_v2.3$  immunogold density is plotted against the dendritic diameter of individual dendritic branches in the PSR. Dendrites can be separated in two different groups (putatively, oblique and primary apical dendrites) based on their dendritic diameter. Mean and SEM of the labeling densities for the two groups are indicated by closed squares and error bars, respectively. Although the immunogold density in individual dendrites were somewhat variable, no difference in the average immunogold density was detected between primary and oblique dendrites ( $p = 0.25$ ; Student's *t* test). **C**, Representative 3D image of a dendritic shaft and its seven daughter spines reconstructed from 19 serial sections. Synaptic contacts are shown in red. The green and pink dots represent the immunogold particles in the spines and shaft, respectively. Immunogold particles at the back side of the structures are not shown. The immunogold particles are distributed throughout the dendritic plasma membrane. Although all seven spines emerge from the same dendrite, a high variability in the number of  $\text{Ca}_v2.3$  particles can be seen among the spines: one spine is strongly immunopositive for  $\text{Ca}_v2.3$ , whereas two others remain immunonegative. Scale cube, 0.2 μm on a side.

spine necks are too small to be resolved well even by two-photon microscopy. Therefore, we examined whether or not  $\text{Ca}_v2.3$  is selectively localized to spine heads. We found that in some spines immunogold particles were localized not only to the head, but also to the neck (Figs. 3A, 4C). When we quantitatively compared the proportion of immunogold particles in head and neck, we found that 413 (83.9%) particles were localized to the head and 79 (16.1%) to the neck of spines ( $n = 119$ ) in the SO. The average number of immunogold particles in the spine head was  $3.5 \pm 0.31$  (median, 2; range, 0–13), whereas in the spine neck it was  $0.7 \pm 0.10$  (median, 0; range, 0–6). In the PSR, 592 immunogold particles were counted in the spines ( $n = 154$ ), of which 468 (79.1%) were localized to the head and 124 (20.9%) were localized to the neck. In the PSR, the average number of immunogold particles found in the spine head and spine neck was  $3.0 \pm 0.27$  (median, 2; range, 0–16) and  $0.8 \pm 0.10$  (median, 0; range, 0–6), respectively. When immunogold particles in the neck and head of dendritic spines were considered, it was found that individual spines contained 0–13 immunogold particles (mean,  $4.1 \pm 0.33$ ; median, 3) in the SO and 0–16 (mean,  $3.8 \pm 0.29$ ; median, 3) in the PSR. These results clearly demonstrate that the  $\text{Ca}_v2.3$  channels were localized not only to the head, but also to the neck, of dendritic spines in the SO and PSR.

### Number of calcium channels in relation to the size of spine head

Synaptic plasticity, occurring at the spine, is dependent on calcium influx through the RTCCs (Yasuda et al., 2003). To explore the relationship between the number of immunogold particles with the spine head surface area and the spine head volume, a total of 119 spines in SO and 154 spines in PSR were examined in serial sections. The surface area and volume of the spines were measured and the total number of immunogold particles in each spine head was determined. The mean surface area of spine heads was  $0.34 \pm 0.018 \mu\text{m}^2$  (median,  $0.29 \mu\text{m}^2$ ; range,  $0.07$ – $1.01 \mu\text{m}^2$ ; total measured area,  $40.43 \mu\text{m}^2$ ) in the SO and  $0.32 \pm 0.018 \mu\text{m}^2$  (median,  $0.23 \mu\text{m}^2$ ; range,  $0.09$ – $1.23 \mu\text{m}^2$ ; total measured area,  $48.98 \mu\text{m}^2$ ) in the PSR. A positive correlation could be found when the number of immunogold particles were plotted against spine head surface area (SO:  $r = 0.72$ ,  $p < 0.01$ ; PSR:  $r = 0.69$ ,  $p < 0.01$ ; data not shown). The larger spines contained more immunogold particles in their spine head, when compared with smaller, thin-type spines. Although the majority of spine heads were found to be immunopositive, ~17% of spine heads in SO and 25% of spine heads in PSR lacked immunogold particle for  $\text{Ca}_v2.3$ .

The average head volume of the spines was  $0.019 \pm 0.001 \mu\text{m}^3$  (median,  $0.015 \mu\text{m}^3$ ; range,  $0.003$ – $0.064 \mu\text{m}^3$ ) in SO and  $0.017 \pm 0.001 \mu\text{m}^3$  (median,  $0.011 \mu\text{m}^3$ ; range,  $0.003$ – $0.082 \mu\text{m}^3$ ) in PSR. The values of the spine head volumes measured in our study closely agree with previously reported data (Harris and Stevens, 1989; Sabatini and Svoboda, 2000; Grunditz et al., 2008; Nicholson and Geinisman, 2009). When the number of immunogold particles in an individual spine head was plotted against their volume, a linear positive correlation was found between these two parameters (SO:  $r = 0.69$ ,  $p < 0.01$ ; PSR:  $r = 0.67$ ,  $p < 0.01$ ; Fig. 6). The regression line had a slope of 183 particles/ $\mu\text{m}^3$  in the SO and 163 particles/ $\mu\text{m}^3$  in the PSR. Despite a positive correlation of the number of immunogold particles with the spine head surface area and spine head volume, there was a large variability in the number of particles even within the spines of similar volume (CVs of the particle density: SO, 0.78; PSR, 0.91; Fig. 6).

To assess the detection sensitivity of our immunogold labeling for  $\text{Ca}_v2.3$ , we also analyzed the immunogold particles in postnatal day 20 rat spines (Figs. 3G, 6C), in which the number and density of RTCCs in spines were estimated using calcium imaging (Sabatini and Svoboda, 2000). When the number of immunogold particles in individual spines was plotted against spine volume, a positive correlation was observed between the immunogold particle number and the spine head volume ( $r = 0.70$ ). The number of immunogold particles in individual spine heads ranged from 0 to 19 in our study and from 1 to 20 in Sabatini and Svoboda's study. The slope of the regression line also compared well be-

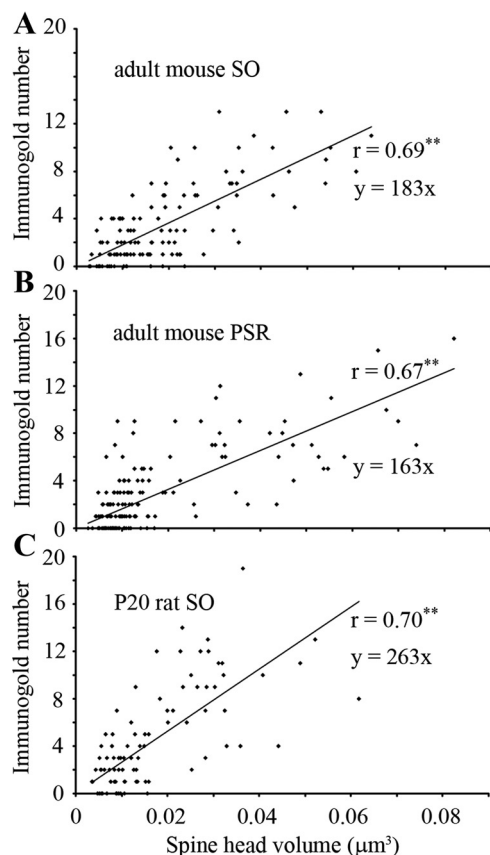


**Figure 6.** Number of  $\text{Ca}_v2.3$  immunoparticles found in individual dendritic spines is positively correlated with the size of spine head. The number of immunogold particles for  $\text{Ca}_v2.3$  in the spine head were plotted against the volume of individual spine heads. The number showed a positive correlation with the spine head volume. **A**, Adult mouse SO,  $r = 0.69$ ,  $n = 119$ ,  $p < 0.01$ , Spearman's rank order test. **B**, Adult mouse PSR,  $r = 0.67$ ,  $n = 154$ ,  $p < 0.01$ , Spearman's rank order test. **C**, Postnatal day 20 (P20) rat,  $r = 0.70$ ,  $n = 84$ ,  $p < 0.01$ , Spearman's rank order test. Note the variability in the number of immunogold particles even among the similarly sized spines.

tween the two studies (our study: 263 particles/ $\mu\text{m}^3$ ; Sabatini and Svoboda's study: 230 channels/ $\mu\text{m}^3$ ; the latter slope value was calculated from the average density of open channels and the average open probability of RTCC as 0.52 reported in the study). Together, these data show that our pre-embedding method has a high sensitivity and gives a reliable indication for the number of  $\text{Ca}_v2.3$  channels.

#### Distance from the PSD

Immunogold particles were found to be localized in and around the PSD of both perforated and nonperforated synapses (Fig. 7A–C). To assess the relative distribution of immunogold particles found in the synaptic and nonsynaptic sites of the PSR spine heads, the lateral distances along the spine head plasma membrane from the closest edge of the PSD to the center of immunogold particles were measured. The distance of particles ( $n = 581$ ) from the edge of the PSD ranged from  $-53.2$  to  $989.4$  nm. When distances were allocated to 60-nm-wide bins and expressed as relative frequency, it was found that the immunogold particles were broadly distributed in the spine head (Fig. 7D). Next, we categorized the immunogold particles as synaptic ( $<0$  nm), perisynaptic ( $0-60$  nm), and extrasynaptic ( $>60$  nm) based on previously defined criteria (Luján et al., 1997). Immunogold particles for  $\text{Ca}_v2.3$  were the most abundant in the extrasynaptic sites

(80.7%, 469 of 581), with some immunogold pools in the perisynaptic (16.0%, 93 of 581) and synaptic sites (3.3%, 19 of 581).

#### Relationship with parent dendrites

Accumulating evidence suggest that spines compartmentalize calcium and operate independently from their parent dendrites (for review, see Yuste et al., 2000). If spines are independent functional compartments, the expression of calcium channels may be regulated intrinsically by the spines regardless of the density in their parent dendrites. Therefore, it is of interest to know whether multiple spines along a single dendritic segment will show any correlation in the labeling density with their parent dendrites. To examine this issue, the average immunogold particle density in the spines, whose parent dendrite was traceable, was plotted against the density in their parent dendrites (Fig. 8). No significant correlation (SO,  $r = -0.19$ ,  $p = 0.17$ , Spearman's rank order test; PSR,  $r = 0.19$ ,  $p = 0.12$ , Spearman's rank order test) could be observed between these two parameters, thereby suggesting an independent expression mechanism of  $\text{Ca}_v2.3$  between dendrites and their spines.

#### Discussion

Our results provide a detailed anatomical characterization of the RTCC pore forming subunit  $\text{Ca}_v2.3$  in distinct subcellular compartments of mouse brain. The major findings are as follows:

1. RTCCs are expressed ubiquitously in the brain with higher levels in the hippocampus, interpeduncular nucleus, striatum, pallidum, cortex, amygdala, olfactory tubercle, accumbens, and dorsal cochlear nucleus than in other regions.
2. RTCCs are predominantly presynaptic in the interpeduncular nucleus, but mainly expressed postsynaptically in other brain regions.
3. RTCCs found in dendritic shafts and spines showed a higher density compared to somata in CA1 of the hippocampus.
4. Individual spine heads contained 0–16  $\text{Ca}_v2.3$  particles in adult mouse and 0–19  $\text{Ca}_v2.3$  particles in postnatal day 20 rat. The latter is consistent with the range of the RTCC number reported previously (Sabatini and Svoboda, 2000).
5. The number of RTCCs in the spine is positively correlated to the spine head volume.
6. The number of RTCCs is highly variable among individual spines.
7. The average density of RTCCs in spine has no correlation to the density in the parent dendrite.

#### General LM distribution of $\text{Ca}_v2.3$

The regional distribution of the  $\text{Ca}_v2.3$  protein described here closely agrees with the previously described *in situ* hybridization patterns (Soong et al., 1993; Williams et al., 1994; Lein et al., 2007). In general, strong immunoreactivity was detected in brain regions where RTCCs have been previously studied using electrophysiological methods (for review, see Weiergräber et al., 2006). However, in regions such as the calyx of Held, the  $\text{Ca}_v2.3$  immunoreactivity was very weak (similar to background level) despite previous electrophysiology experiment (Wu et al., 1999) suggesting their presence. The strong immunoreactivity in the thalamus and the prominent somatic staining in various brain regions reported by Yokoyama et al. (1995) were also not observed in our study. The discrepancy between Wu's observations and ours may



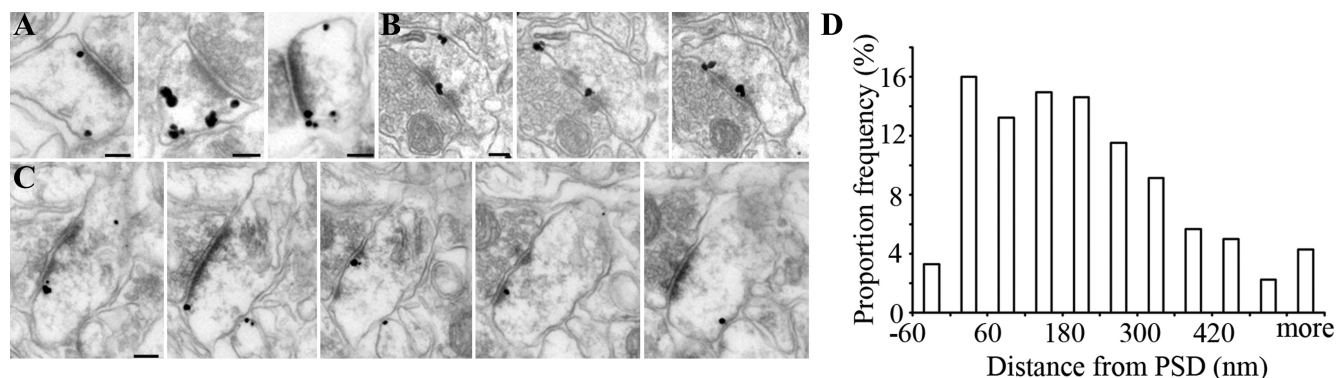


**Figure 7.**  $\text{Ca}_v2.3$  channels are localized throughout the spine head plasma membrane. Electron micrographs showing immunoreactivity for  $\text{Ca}_v2.3$  at the synaptic, perisynaptic, and extrasynaptic plasma membrane of dendritic spine head. **A–C**, Both in thin (**A**, SO, left and middle; PSR, right) and mushroom spines (**B**, SO; **C**, PSR), immunogold particles are localized in the vicinity as well as remote from the edge of the PSD. **D**, Histogram showing the lateral distances of immunogold particles for  $\text{Ca}_v2.3$  ( $n = 581$ ) measured from the nearest edge of the PSD. The nearest edge of the PSD is defined as zero. The distance was expressed as a negative value if particles were located along the plasma membrane within the main body of the PSD and as a positive value if immunogold particles were seen on the extrasynaptic plasma membrane. Each bin represents 60 nm. Immunogold particles are broadly distributed within the spine head. Scale bars, 100 nm.

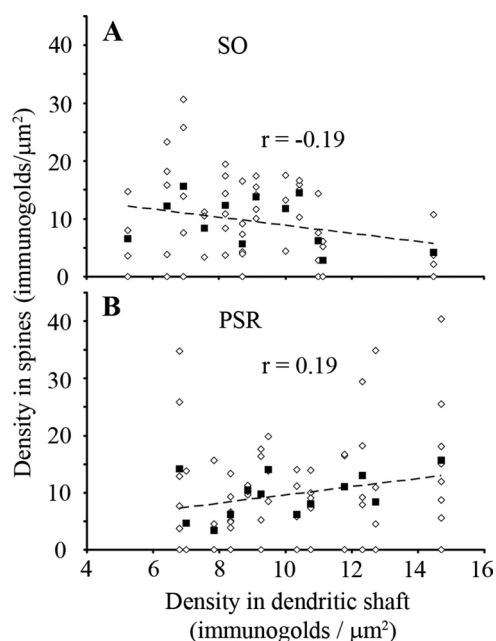


**Figure 8.** Average immunogold density for  $\text{Ca}_v2.3$  among spines is independent from the density in the parent dendritic shaft. **A**, **B**, Scatter plots show the labeling density for  $\text{Ca}_v2.3$  in individual spines (open diamond) in SO (**A**,  $n = 56$ ) and PSR (**B**,  $n = 66$ ) as a function of the labeling density in their mother dendritic shafts (SO,  $n = 12$ ; PSR,  $n = 13$ ). In both of the regions, the labeling density for  $\text{Ca}_v2.3$  varies among dendrites. Also, the average labeling density in the spines (closed square) is not correlated with that in the mother dendrites (SO,  $r = -0.19$ ,  $p = 0.17$ , Spearman's rank order test; PSR,  $r = 0.19$ ,  $p = 0.12$ , Spearman's rank order test).

have arisen from other subunits forming the RTCC current in the calyx of Held. It is important to note that R-type current could still be recorded in such neurons as the cerebellar granule cells and the dorsal root ganglion cells of  $\text{Ca}_v2.3$  KO mice (Wilson et al., 2000). The difference in the age of the experimental animals may also account for the discrepancy. For example, in contrast to our study, which focused on adult mice, Wu et al.'s study was done in 8–10-d-old rats. Interestingly, Iwasaki et al. (2000) have described P/Q-, N- and R-type VGCC in the calyx terminal of postnatal day 10 rats, but only P/Q-type in postnatal day 13. This further substantiates the developmental changes as a cause of the discrepancy between two studies.

### Detection sensitivity of our immunolabeling method

Immunogold labeling methods are generally thought to underestimate the total number of target molecules. The degree of underestimation may vary depending upon the target molecules and the immunogold localization technique used (for review, see Masugi-Tokita and Shigemoto, 2007). To validate the immunolabeling efficiency, functional analysis of the target molecules must be compared with the number of immunoparticles detected. Quantification using the  $\text{Ca}_v2.3$  antibody correlated well with the number of channels in individual spines previously reported using optical fluctuation analysis (our study: range, 0–19; slope, 263 particles/ $\mu\text{m}^2$ ; Sabatini and Svoboda's study (2000): range, 1–20; slope, 230 channels/ $\mu\text{m}^2$ ). However, we found some spines showing no immunoreactivity for  $\text{Ca}_v2.3$ . These  $\text{Ca}_v2.3$  negative spines may not have been reported by Sabatini and Svoboda because spines whose variance in fluorescence was not different from the dark noise were excluded from their analysis. As a result of the high detection sensitivity for  $\text{Ca}_v2.3$  with the pre-embedding immunogold labeling method, our present study provides a reliable estimate for the *in situ* density of RTCCs in the neuronal plasma membrane.

### $\text{Ca}_v2.3$ in postsynaptic compartment

Our study revealed heterogeneity in the number of RTCCs expressed among dendritic spines (Fig. 5A,C). This heterogeneity may stem from intrinsic properties of the given spine or differences in cell lineages from which the spine originates. It is unlikely that the cell lineage dictates differential expression because even the spines protruding from the same dendrite display large variability (Fig. 8). It is more probable that the individual spine characteristics, such as age or plasticity, contribute to differential expression of RTCCs in spines. Regardless of the source of variability, our results support the idea that spines are individual biochemical compartments operating autonomously from their parent dendrites (for review, see Yuste et al., 2000).

Matsuzaki et al. (2004) have demonstrated that only a subpopulation of the spines, specifically the thin type, are susceptible to induction of long-term potentiation. To date, the molecular mechanism governing this phenomenon still remains elusive. It has been previously shown that the activation of SK2 channels, which would dampen the membrane depolarization, require calcium entry through both NMDA receptors and RTCCs (Bloodgood and Sabatini, 2007). Previous immunohistochemical (Takumi et al., 1999) and functional (Noguchi et al., 2005) stud-

ies have suggested that all spines are equipped with NMDA receptors and the number of NMDA receptors do not correlate with either the size of the synapses or with the spine volume. However, our results showed that the number of RTCCs increases with the spine volume, and the subpopulation of thin-type spines lacked RTCCs. Although the functional relevance of our observation remains to be experimentally tested, we envisage that the spines lacking RTCCs are susceptible to potentiation because of the inability to activate SK2 channels. Some thin spines and all larger spines that contain high numbers of RTCCs are less likely to be potentiated because RTCC opening in these spines leads to SK-channel activation, which in turn would dampen changes in the membrane potential.

NMDARs and VGCCs, in particular the R-type, are the major sources of calcium influx into hippocampal spines. It is interesting to note that these two differ in terms of their ultrastructural localization in the spines, which suggests a distinct role of these channels in the spines. NMDA receptors are strictly concentrated in the PSD (Takumi et al., 1999), while RTCCs are rather abundant at the extrasynaptic plasma membrane. However, we cannot exclude underestimation of the  $\text{Ca}_v2.3$  labeling due to the limited access of antibodies to PSD in the pre-embedding method (for review, see Masugi-Tokita and Shigemoto, 2007). The restriction of NMDARs to the PSD (i.e., in opposition to the AZ) is important for faithful activation of the receptors by glutamate released at the AZ. However, there exists no necessity for the RTCC to be restricted to the PSD because the membrane depolarization created by the voltage change, which is required for RTCC opening, rapidly propagates throughout the spine head plasma membrane. The differential localization between these two spine head calcium sources also argue for their unique access to downstream effectors. The observed distribution pattern of  $\text{Ca}_v2.3$  would also be beneficial for the activation of SK channels as they are also known to be present throughout the spine heads (Lin et al., 2008).

### $\text{Ca}_v2.3$ in presynaptic compartment

The strong immunoreactivity for  $\text{Ca}_v2.3$  of the MHb terminals in the IPN is an interesting finding and is in sharp contrast to its predominant postsynaptic localization in other brain regions. Postsynaptic RTCCs have been suggested to play a major role in regulation of synaptic plasticity and dendritic excitability, but little information is available regarding the function of presynaptic R-type channels. Although no brain nuclei to date has been shown to have purely R-type channel-mediated neurotransmitter release, this unique expression pattern of R-type channels in IPN warrants future experiments to determine their role in vesicular release in this nucleus. Interestingly, no mRNA transcripts for P/Q-type and N-type channels could be detected in the MHb (Ludwig et al., 1997). Thus, the future study of the MHb-IPN pathway may open the possibility to reveal the biophysical properties and the functional roles of R-type channels in isolation.

In the IPN, immunogold particles were mainly observed at the extrasynaptic plasma membrane and only occasionally over the presynaptic AZ, indicating a distinct distribution pattern compared with  $\text{Ca}_v2.1$  (Kulik et al., 2004; Holderith et al., 2012). This may suggest that RTCCs may play specialized functional roles, in addition to their role in neurotransmitter release, in the presynaptic compartments. For example, activation of presynaptic BK channels in the IPN (Knaus et al., 1996) by  $\text{Ca}_v2.3$  may function to modulate an action potential. In all regions examined where  $\text{Ca}_v2.3$  was localized to the presynaptic compartment,  $\text{Ca}_v2.3$  immunogold particles were mainly seen to be remote from the AZ,

indicating that this is a common organizational scheme of this channel in the presynaptic compartment.

In conclusion, our study provides a novel understanding of the unique presynaptic and postsynaptic localization of the  $\text{Ca}_v2.3$  subunit in the brain.

### References

- Augustine GJ, Santamaria F, Tanaka K (2003) Local calcium signaling in neurons. *Neuron* 40:331–346.
- Báldi R, Varga C, Tamás G (2010) Differential distribution of KCC2 along the axo-somato-dendritic axis of hippocampal principal cells. *Eur J Neurosci* 32:1319–1325.
- Bloodgood BL, Sabatini BL (2007) Nonlinear regulation of unitary synaptic signals by  $\text{Ca}_v2.3$  voltage-sensitive calcium channels located in dendritic spines. *Neuron* 53:249–260.
- Bourne JN, Harris KM (2008) Balancing structure and function at hippocampal dendritic spines. *Annu Rev Neurosci* 31:47–67.
- Day NC, Shaw PJ, McCormack AL, Craig PJ, Smith W, Beattie R, Williams TL, Ellis SB, Ince PG, Harpold MM, Lodge D, Volsen SG (1996) Distribution of  $\alpha1A$ ,  $\alpha1B$  and  $\alpha1E$  voltage-dependent calcium channel subunits in the human hippocampus and parahippocampal gyrus. *Neuroscience* 71:1013–1024.
- Fiala JC (2005) Reconstruct: a free editor for serial section microscopy. *J Microsc* 218:52–61.
- Frick A, Magee J, Koester HJ, Migliore M, Johnston D (2003) Normalization of  $\text{Ca}^{2+}$  signals by small oblique dendrites of CA1 pyramidal neurons. *J Neurosci* 23:3243–3250.
- Gasparini S, Kasyanov AM, Pietrobon D, Voronin LL, Cherubini E (2001) Presynaptic R-type channels contribute to fast excitatory synaptic transmission in the rat hippocampus. *J Neurosci* 21:8715–8721.
- Giessel AJ, Sabatini BL (2011) Boosting of synaptic potentials and spine  $\text{Ca}^{2+}$  transients by the peptide toxin SNX-482 requires  $\alpha1E$ -encoded voltage-gated  $\text{Ca}^{2+}$  channels. *PLoS One* 6:e20939.
- Grunditz A, Holbro N, Tian L, Zuo Y, Oertner TG (2008) Spine neck plasticity controls postsynaptic calcium signals through electrical compartmentalization. *J Neurosci* 28:13457–13466.
- Harris KM, Stevens JK (1989) Dendritic spines of CA1 pyramidal cells in the rat hippocampus: serial electron microscopy with reference to their biophysical characteristics. *J Neurosci* 9:2982–2997.
- Holderith N, Lorincz A, Katona G, Rózsa B, Kulik A, Watanabe M, Nusser Z (2012) Release probability of hippocampal glutamatergic terminals scales with the size of the active zone. *Nat Neurosci* 15:988–997.
- Iwasaki S, Momiyama A, Uchitel OD, Takahashi T (2000) Developmental changes in calcium channel types mediating central synaptic transmission. *J Neurosci* 20:59–65.
- Knaus HG, Schwarzer C, Koch RO, Eberhart A, Kaczorowski GJ, Glossmann H, Wunder F, Pongs O, Garcia ML, Sperk G (1996) Distribution of high-conductance  $\text{Ca}^{2+}$ -activated  $\text{K}^{+}$  channels in rat brain: targeting to axons and nerve terminals. *J Neurosci* 16:955–963.
- Kulik A, Nakadate K, Hagiwara A, Fukazawa Y, Luján R, Saito H, Suzuki N, Futatsugi A, Mikoshiba K, Frotscher M, Shigemoto R (2004) Immunocytochemical localization of the  $\alpha1A$  subunit of the P/Q-type calcium channel in the rat cerebellum. *Eur J Neurosci* 19:2169–2178.
- Lein ES, Hawrylycz MJ, Ao N, Ayres M, Bensinger A, Bernard A, Boe AF, Boguski MS, Brockway KS, Byrnes EJ, Chen L, Chen L, Chen TM, Chin MC, Chong J, Crook BE, Czaplinska A, Dang CN, Datta S, Dee NR, et al. (2007) Genome-wide atlas of gene expression in the adult mouse brain. *Nature* 445:168–176.
- Lenn NJ (1976) Synapses in the interpeduncular nucleus: electron microscopy of normal and habenula lesioned rats. *J Comp Neurol* 166:77–99.
- Lin MT, Luján R, Watanabe M, Adelman JP, Maylie J (2008) SK2 channel plasticity contributes to LTP at Schaffer collateral-CA1 synapses. *Nat Neurosci* 11:170–177.
- Lörincz A, Notomi T, Tamás G, Shigemoto R, Nusser Z (2002) Polarized and compartment-dependent distribution of HCN1 in pyramidal cell dendrites. *Nat Neurosci* 5:1185–1193.
- Ludwig A, Flockerzi V, Hofmann F (1997) Regional expression and cellular localization of the  $\alpha1$  and  $\beta$  subunit of high voltage-activated calcium channels in rat brain. *J Neurosci* 17:1339–1349.
- Luján R, Roberts JD, Shigemoto R, Ohishi H, Somogyi P (1997) Differential plasma membrane distribution of metabotropic glutamate receptors



- mGluR1  $\alpha$ , mGluR2 and mGluR5, relative to neurotransmitter release sites. *J Chem Neuroanat* 13:219–241.
- Masugi-Tokita M, Shigemoto R (2007) High-resolution quantitative visualization of glutamate and GABA receptors at central synapses. *Curr Opin Neurobiol* 17:387–393.
- Matsubara A, Laake JH, Davanger S, Usami S, Ottersen OP (1996) Organization of AMPA receptor subunits at a glutamate synapse: a quantitative immunogold analysis of hair cell synapses in the rat organ of Corti. *J Neurosci* 16:4457–4467.
- Matsuzaki M, Honkura N, Ellis-Davies GC, Kasai H (2004) Structural basis of long-term potentiation in single dendritic spines. *Nature* 429:761–766.
- Megias M, Emri Z, Freund TF, Gulyás AI (2001) Total number and distribution of inhibitory and excitatory synapses on hippocampal CA1 pyramidal cells. *Neuroscience* 102:527–540.
- Nicholson DA, Geinisman Y (2009) Axospinous synaptic subtype-specific differences in structure, size, ionotropic receptor expression, and connectivity in apical dendritic regions of rat hippocampal CA1 pyramidal neurons. *J Comp Neurol* 512:399–418.
- Noguchi J, Matsuzaki M, Ellis-Davies GC, Kasai H (2005) Spine-neck geometry determines NMDA receptor-dependent  $\text{Ca}^{2+}$  signaling in dendrites. *Neuron* 46:609–622.
- Nusser Z (2009) Variability in the subcellular distribution of ion channels increases neuronal diversity. *Trends Neurosci* 32:267–274.
- Parajuli LK, Fukazawa Y, Watanabe M, Shigemoto R (2010) Subcellular distribution of  $\alpha 1G$  subunit of T-type calcium channel in the mouse dorsal lateral geniculate nucleus. *J Comp Neurol* 518:4362–4374.
- Pereverzev A, Mikhna M, Vajna R, Gissel C, Henry M, Weiergräber M, Hescheler J, Smyth N, Schneider T (2002) Disturbances in glucose-tolerance, insulin-release and stress-induced hyperglycemia upon disruption of the  $\text{Ca}_v2.3$  ( $\alpha 1E$ ) subunit of voltage-gated  $\text{Ca}^{2+}$  channels. *Mol Endocrinol* 16:884–895.
- Peters A, Palay S, Webster H (1991) The fine structure of the nervous system: neurons and their supporting cells. New York: Oxford UP.
- Sabatini BL, Svoboda K (2000) Analysis of calcium channels in single spines using optical fluctuation analysis. *Nature* 408:589–593.
- Sabatini BL, Oertner TG, Svoboda K (2002) The life cycle of  $\text{Ca}^{2+}$  ions in dendritic spines. *Neuron* 33:439–452.
- Saegusa H, Kurihara T, Zong S, Minowa O, Kazuno A, Han W, Matsuda Y, Yamanaka H, Osanai M, Noda T, Tanabe T (2000) Altered pain responses in mice lacking  $\alpha 1E$  subunit of the voltage dependent  $\text{Ca}^{2+}$  channel. *Proc Natl Acad Sci U S A* 97:6132–6137.
- Sochivko D, Pereverzev A, Smyth N, Gissel C, Schneider T, Beck H (2002) The  $\text{Ca}_v2.3$   $\text{Ca}^{2+}$  channel subunit contributes to R-type  $\text{Ca}^{2+}$  currents in murine hippocampal and neocortical neurones. *J Physiol* 542:699–710.
- Soong TW, Stea A, Hodson CD, Dubel SJ, Vincent SR, Snutch TP (1993) Structure and functional expression of a member of the low voltage-activated calcium channel family. *Science* 260:1133–1136.
- Svoboda K, Tank DW, Denk W (1996) Direct measurement of coupling between dendritic spines and shafts. *Science* 272:716–719.
- Takahashi H, Magee JC (2009) Pathway interactions and synaptic plasticity in the dendritic tuft regions of CA1 pyramidal neurons. *Neuron* 62:102–111.
- Takumi Y, Ramírez-León V, Laake P, Rinvik E, Ottersen OP (1999) Different modes of expression of AMPA and NMDA receptors in hippocampal synapses. *Nat Neurosci* 2:618–624.
- Tottene A, Volsen S, Pietrobon D (2000)  $\alpha 1E$  subunits form the pore of three cerebellar R-type calcium channels with different pharmacological and permeation properties. *J Neurosci* 20:171–178.
- Trommald M, Jensen V, Andersen P (1995) Analysis of dendritic spines in rat CA1 pyramidal cells intracellularly filled with a fluorescent dye. *J Comp Neurol* 353:260–274.
- Weiergräber M, Kamp MA, Radhakrishnan K, Hescheler J, Schneider T (2006) The  $\text{Ca}_v2.3$  voltage-gated calcium channel in epileptogenesis—shedding new light on an enigmatic channel. *Neurosci Biobehav Rev* 30:1122–1144.
- Williams ME, Marubio LM, Deal CR, Hans M, Brust PF, Philipson LH, Miller RJ, Johnson EC, Harpold MM, Ellis SB (1994) Structure and functional characterization of neuronal  $\alpha 1E$  calcium channel subtypes. *J Biol Chem* 269:22347–22357.
- Wilson SM, Toth PT, Oh SB, Gillard SE, Volsen S, Ren D, Philipson LH, Lee EC, Fletcher CF, Tessarollo L, Copeland NG, Jenkins NA, Miller RJ (2000) The status of voltage-dependent calcium channels in  $\alpha 1E$  knockout mice. *J Neurosci* 20:8566–8571.
- Wu LG, Westenbroek RE, Borst JG, Catterall WA, Sakmann B (1999) Calcium channel types with distinct presynaptic localization couple differentially to transmitter release in single calyx-type synapses. *J Neurosci* 19:726–736.
- Yasuda R, Sabatini BL, Svoboda K (2003) Plasticity of calcium channels in dendritic spines. *Nat Neurosci* 6:948–955.
- Yokoyama CT, Westenbroek RE, Hell JW, Soong TW, Snutch TP, Catterall WA (1995) Biochemical properties and subcellular distribution of the neuronal class E calcium channel  $\alpha 1$  subunit. *J Neurosci* 15:6419–6432.
- Yuste R, Majewska A, Holthoff K (2000) From form to function: calcium compartmentalization in dendritic spines. *Nat Neurosci* 3:653–659.